Vibrational and electronic structures of tin selenide nanowires confined inside carbon nanotubes

Eric Faulques, Nataliya Kalashnyk, Charlotte Slade, Ana Sanchez, Jeremy Sloan, Victor Ivanov

Vibrational and electronic structures of tin selenide nanowires confined inside carbon nanotubes

Eric Faulques*,[1], Nataliya Kalashnyk[2], Charlotte A. Slade[3], Ana M. Sanchez[3], Jeremy Sloan[3] and Victor G. Ivanov[4]

Address: [1]University of Nantes, CNRS, Institut des Matériaux Jean Rouxel, IMN, F-44000 Nantes, France; [2]Laboratoire de Physique des Matériaux et des Surfaces, CY Cergy Paris University, Rue d'Eragny, Neuville sur Oise, F-95031 Cergy-Pontoise, France; [3]Department of Physics, University of Warwick, Gibbet Hill Road, Coventry CV4 7AL, United Kingdom and [4]Sofia University, Faculty of Physics, 5 James Bourchier Blvd., 1164 Sofia, Bulgaria

Email: Eric Faulques - eric.faulques@cnrs-imn.fr

* Corresponding author

Abstract

We study vibrational and electronic properties of tin selenide (SnSe) nanowires encapsulated in single walled carbon nanotubes (SWCNT) by combining experimental Raman spectroscopy and density functional theory (DFT) calculations at the Heyd-Scuseria-Ernzerhof (HSE) level. The theoretically investigated standalone SnSe nanowires are Sn_4Se_4 with square (2×2) atomic arrangement and Sn_6Se_6 with a repeating hexagonal Mo_6S_6-like structure. Raman data support the theoretical prediction that the square (2×2) nanowires possess specific modes at 151 and 185 cm^{-1}, whereas the hexagonal Sn_6Se_6 structure is characterized by a mode appearing at ~235 cm^{-1}. Calculations predict that the (2×2) nanowire has an electronic gap of 1.5 eV and the Sn_6Se_6 nanowire presents a semi-metallic character. Raman spectra of composite SnSe@SWCNT samples show that the radial breathing mode of the nanotubes is strongly suppressed indicating interaction between SWCNT and the encapsulated SnSe nanowire while the Fano asymmetry parameter of the *G* band is increased.

Keywords

carbon nanotubes, tin telluride, Raman spectroscopy, phonons, electrons, *ab-initio* calculations

1 Introduction

Inorganic and organic nanowires and nanostructured materials like nanorods or nanoplates are a topic of utmost importance in many studies of physics, chemistry, biology, and medicine. The mechanical, electrical, electronic, magnetic, and chemical properties of these nano-objects can differ considerably from those of the parent bulk materials leading to applications for storage devices, electronic chips, photovoltaics, batteries, and therapeutic processes [1-7].

In particular, tin selenide, SnSe, is an important binary chalcogenide material which displays remarkable electronic, thermoelectric, and optoelectronic properties depending on its morphology as bulk crystal, thin films, or low-dimensional nanostructures [8]. This material can be applied notably for photovoltaics, anodes in rechargeable batteries, supercapacitors, phase-change memory devices, and topological insulators. Bulk tin(II) selenide is a narrow band-gap (IV-VI) semiconductor with both indirect and direct band gaps of 0.9 eV and 1.3 eV, respectively. The bulk chalcogenide crystal has an accordion-like stacked two-dimensional (2D) structure that gives it low anharmonicity and low lattice thermal conductivity making it a poor thermal conductor while its ZT factor of merit has a high temperature value of 2.6 [9],[10].

Single-walled carbon nanotubes (SWCNT) are low-dimensional allotropes of carbon which have unique mechanical, electronic and optical properties depending on their morphology [11]. As expected for one-dimensional (1D) systems, they present van Hove singularities in the density of states whose energies vary with the diameter and length of the nanotube. Depending on their chirality SWCNTs are either metallic or semi-conductors allowing their application in flexible electronic devices, lithium battery anodes, flat panel displays, sensors, supercapacitors, drug delivery, and STM/AFM tips [12,13]. Therefore, binary chalcogenides combined with SWCNTs can give rise to very unusual physical properties in the as-grown composites, but also this can foster drastic changes in the electronic properties of either component. Recently, several binary chalcogenides

have been encapsulated in both single-walled and double-walled carbon nanotubes (DWCNT) resulting in unique 1D chalcogenide crystalline wires with diameter comparable to a unit cell of the 3D crystal [14-17]. Due to their extreme low lateral size and specific atomic arrangement, the physical properties of these confined and atomically constrained nanowires are expected to be significantly different from those of the corresponding parent bulk materials.

Here we present a detailed comparative study of the structural, electronic, and vibrational properties of two original nanostructures of atom-sized SnSe nanowires encapsulated in SWCNTs. Previous high-resolution transmission electron microscopy (HRTEM) investigations have shown that SnSe crystallizes into (2×2)-atom per cross section structure inside SWCNTs, adopting the same atomic arrangement as earlier described 1D (2×2) KI nanocrystals, hereafter referred to as Sn_4Se_4, embedded in double-walled or single-walled carbon nanotubes [14]. Recently, a novel 1D hexagonal SnSe crystalline form was discovered in SWCNTs [18] with an Mo(S,Se)-type of coordination environment [19,20], hereafter referred to as Sn_6Se_6, comprising three Sn atoms and three Se atoms per constituent layer, which is not observed in any of the other low-dimensional forms of the selenium chalcogenides. Interestingly, Nagata *et al.* [17] reported also similar MoTe nanowires structures in SWNTs. Previous DFT simulations predict a metallic nature of hexagonal MX nanowires with M=Mo,W and W=S,Se [21,22] but semiconducting properties for the isostructural Cr_6Te_6 compound [21]. Both, theoretical simulations and experiments, confirm the structural stability of the stand-alone Mo(S,Se) nanowires, which were found as effective nanoscale electrical connectors between $Mo(S,Se)_2$ monolayers [19,20]. In this aspect the physical properties of the isostructural Sn-based nanowires are far from understanding, and our work has been motivated by the following questions:

(i) Are the $Sn_4Se_4$and Sn_6Se_6 nanowires structurally stable, or can they exist only encapsulated in SWCNTs?

(ii) Are the two types of nanowires semiconducting or metallic? While Carter *et al.* previously predicted a gaped band structure for Sn_4Se_4 nanowire using different functional and pseu-

dopotentials [16], electronic properties of the then unobserved Sn_6Se_6 1D crystal were not determined.

(iii) What are the vibrational modes of both Sn_4Se_4 and Sn_6Se_6 nanowires which could give signatures in Raman spectra of SnSe@SWNT composites? This question was not treated up to now.

(iv) What is the impact of encapsulation of the SnSe material on the physical properties of the surrounding nanotubes with matching diameter, e. g. metallic or semiconducting character ?

We addressed the first problems theoretically by means of extensive DFT calculations of the equilibrium structure, electronic band structure, and vibrational eigenmodes for the two forms of SnSe nanowires. In order to assess the last two questions, we studied experimentally the Raman spectra of SnSe@SWCNT composites. Raman spectroscopy has proven to be a very efficient tool for characterizing SWCNTs embedding 1D atom-sized crystalline HgTe and KI nanowires [23,24]. In both cases it has been demonstrated that it is possible to identify several intrinsic vibrational modes of the nanowires superimposed with the Raman spectrum of SWCNTs. By following the same methodology here we study the in-situ dynamics of the embedded SnSe nanocrystals and their interactions with the nanotube walls. The radial breathing mode (RBM) and longitudinal vibrational modes (G-band) of the surrounding nanotubes are found to be strongly affected by the presence of the encapsulated material, which leads us to important conclusions concerning the electronic properties of the SnSe@SWCNT composites corroborating the DFT predictions.

2 Experimental methods and calculation details

The SnSe@SWCNT samples were fabricated using infiltration protocols described previously [16,18]. In this set of experiments, commercial SWCNTs from NanoIntegris PureTubes (99% pure, 1.2-1.7 nm diameter, 300 nm to 5 μm length) were used to encapsulate tin selenide. Here, the SWCNTs were washed, dissolved in N- Methyl-2-pyrrolidone (NMP), dried, pre-heated to 1173 K to remove solvent and to open the tubes. The nanotubes were filled by the modified high

yield molten-phase capillarity technique adapted for SnSe filling. SWCNTs were intimately ground with SnSe (99.995%, Sigma Aldrich), and heated in pure silica quartz tubes sealed under vacuum to 100 K above the melting point of SnSe at around 1233 K.

Micro-Raman experiments were performed with Horiba Jobin-Yvon LabRAM HR 800 Vis and Renishaw inVia Reflex Raman microscope spectrometers in single monochromator mode with diffraction gratings of 600 and 1200 grooves/mm, respectively. Laser excitations λ_{exc} = 633 and 785 nm (1.96 and 1.58 eV) were provided by helium-neon and diode lasers, respectively. Spectra were collected at room temperature in the range between 100 and 3000 cm^{-1} allowing the simultaneous registration of the spectra of the fillers and the carbon nanotubes. The diameter and power of the laser spot on the sample surface were 2 μm, 200 μW (LabRAM) and 45 μW (Renishaw) respectively, for the fully focused laser beam with 50× objective magnification. The SnSe@SWCNT samples were generally found to be homogeneous under microscope without the presence of significant amounts of extraneous SnSe amorphous or microcrystalline phase materials. Raman instruments were calibrated against the Stokes Raman signal of pure Si at 520.5 cm^{-1} using a silicon wafer. The spectral resolution was 2 cm^{-1}. In each experiment, several spectra were recorded on different spots in the samples. The Raman spectra of three characteristic composite SnSe@SWCNT samples, # 1, # 2, and # 3 are presented and compared to those of SWCNT pristine samples.

The DFT calculations were performed with the Cambridge Serial Total Energy Package (CASTEP) plane wave code [25] by making use of Heyd-Scuseria-Ernzerhof screened Coulomb hybrid exchange-correlation functional HSE06 with 1/4 Hartree-Fock exchange [26] and norm-conserving pseudopotentials for the core electrons. The choice of this functional was motivated by a better geometry optimization of the Sn_6Se_6 nanowire and calculation of the vibrational frequencies without imaginaries. It is also reported in the literature that HSE06 yields improved prediction of band gap energy and correct band structure in semiconductors [26]. HSE was also described to be well suited for calculating the phonon frequencies [26-29]. The plane-wave energy cutoff was set mainly at 440 eV (32.34 Ry), and in some cases at 350 and 400 eV. The self-consistent calculations for the 1D Sn_4Se_4 and Sn_6Se_6 nanowires were performed on $1 \times 1 \times 2$ and $1 \times 1 \times 6$ Monkhorst-Pack

(MP) k-point mesh, respectively. We assessed the chosen DFT scheme by performing test calculations for the bulk tin selenide on a $1 \times 3 \times 3$ MP grid. Electronic convergence threshold for energy was set to be $0.5{\times}10^{-6}$ eV. The optimization of cell parameters was allowed to proceed by keeping original symmetry with a total energy convergence tolerance of $0.5{\times}10^{-5}$ eV/atom and until the force on each atom was less than 10 meV/Å. Phonon calculations were carried out at HSE level using exclusively the finite displacement (FD) method in a supercell since the linear response scheme (Density Functional Perturbation Theory, DFPT) was not implemented with hybrid functionals in this DFT code.

3 Results and discussion

Experimental Raman spectra are discussed after the subsection of SnSe nanowires calculations. The spectra were recorded on several pristine and composite SWCNT samples. We sorted among these spectra those of three SnSe@SWCNT composites referred to as # 1, # 2, and # 3. They mainly differ from each other in the low frequency region characteristic of the RBM modes of the SWCNT molecular containers and of possible lines stemming from the SnSe encapsulated crystals. Spectra labelled # 0 are from the pristine SWCNT phase. Fig. 1 shows high-resolution transmission electron microscopy images (HRTEM) of the investigated SnSe filled samples. These images confirm both the high filling fraction of SnSe in 'NanoIntegris' SWCNTs but also the composition of the encapsulated material.

3.1 Predictive calculations for stand-alone SnSe nanowires

This section is devoted to the calculation and analysis of 1D SnSe nanowires. The final relaxed structures are given, and the phonons are calculated after geometry optimization. The Γ-point modes are classified with their different symmetries, and sorted by frequencies. Meanwhile, the electronic band structures of the standalone nanowires are presented and discussed.

3.1.1 Relaxed geometries

The geometries are entirely based on experimental HRTEM images realized on our samples [16,18] (see right panel in Fig. 1) and were chosen as those of infinite rods along the [001] direction relative to a bulk cubic rocksalt unit cell with 2×2 and 3+3 SnSe cross sections, corresponding to square NaCl-like and hexagonal MoSe-like coordinations, respectively. The starting crystal parameters of the Sn_4Se_4 nanowire rely on HRTEM measurements by Carter *et al.* [16]. The initial distances in the hexagonal Sn_6Se_6 nanowire were set arbitrarily at values close to those of the layered *Pnma* bulk crystal with a translation period of c ∼5 Å [30].

In order to perform the calculations with a plane wave (PW) basis set, periodic boundary conditions were imposed along the *a* and *b* axes of the nanowires with a period of 10 Å. The geometry optimization of the nanowires converges to the two structures shown in Fig. 1. The optimized translation period c along the nanowire axis is 5.708 Å and 4.324 Å for Sn_4Se_4 and Sn_6Se_6 nanowires, respectively. Some relevant interatomic distances for the two nanowires are shown in Fig. 1 and are listed in more detail in Table 1. Note that the Sn-Se distances of the Sn_6Se_6 relaxed nanowire match well those found by Slade *et al.* in HRTEM images [18].

The rod symmetry elements of the two nanowires consist of a fourfold 4_2 or a sixfold 6_3 screw axis along c, of mirror planes m parallel to the ***ab*** and ***bc*** planes, an inversion center, and glide planes parallel to ***ac*** and ***bc*** planes with $1/2$ translation of $c/2$ (Fig. 1). Therefore, the Sn_4Se_4 structure can be described by the rod symmetry group $p4_2/mmc$ (No. 41) with all atoms occupying 4d Wyckoff positions. The Sn_6Se_6 structure can be described as a periodic stack of equilateral Sn_3Se_3 triangles. The triangles in the consecutive layers are rotated around the c-axis at 180° relative to each other, as shown in Fig. 1(c)-(d). Thus, the periodicity of the Sn_6Se_6 structure corresponds to the doubled interlayer spacing, and the structure is described by the rod symmetry group $p6_3/mmc$ (No. 75) with all atoms occupying 6d Wyckoff positions.

[ht]

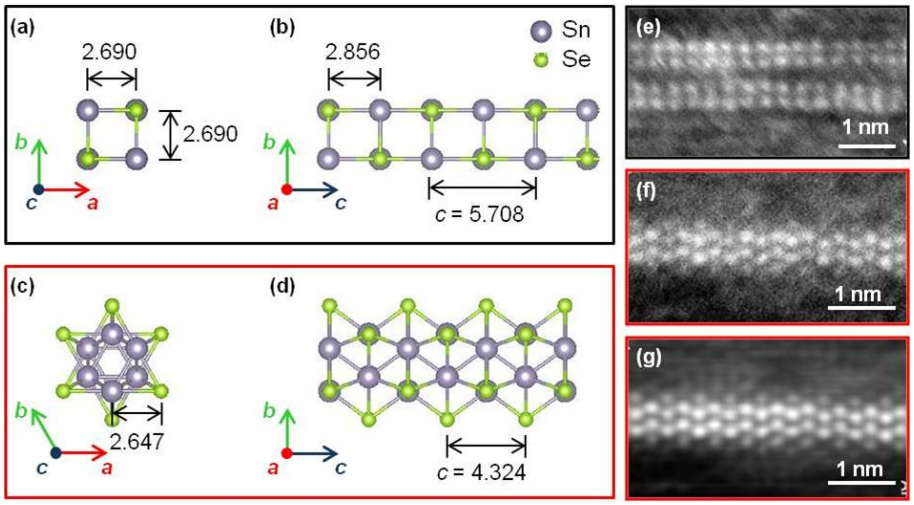

Figure 1: Left panel: Optimized structure of the two SnSe nanowires using the HSE hybrid functional. Vector **c** is parallel to the nanowire axis. Vectors **a** and **b** represent the translation periods of the surrounding superlattice and are parallel to the SnSe layers. All distances are in Angstroms. The 2×2 SnSe crystal of *p4$_2$/mmc* symmetry: views along the nanowire axis (a) and parallel to the Sn_2Se_2 layers (b). The hexagonal Sn_6Se_6 crystal of *p6$_3$/mmc* symmetry: views along the nanowire axis (c) and parallel to the Sn_3Se_3 layers (d). Right panel: (e) experimental HRTEM annular dark field (ADF) image of a pair of 2x2 SnSe crystals observed in a representative SWCNT sample; (f) and (g) unfiltered and adaptive filtered ADF images of an encapsulated Sn_6Se_6 crystal observed in the same representative SWCNT sample.

3.1.2 Normal modes of vibrations

The normal modes of vibrations were calculated for the optimized structures at the Γ-point and along the $\Gamma - Z$ direction for the Sn_4Se_4 nanowire. A one-dimensional acoustic sum rule was imposed on the dynamical matrix in order to account for the four zero-frequency modes of a freely standing nanowire: the three free translations and also the free rotation about the *c* axis. Since the unit cells of the Sn_4Se_4 and Sn_6Se_6 nanowires contain 8 and 12 atoms respectively, their corresponding phonon spectra consist of 24 and 36 dispersion branches along the Γ-Z direction. The normal modes of the Sn_4Se_4 and Sn_6Se_6 nanowire at the Γ-point are classified according to the irreducible representations of the *4/mmm* (D_{4h}) and *6/mmm* (D_{6h}) point groups. The symmetry decomposition was performed with the aid of SAM software available on the Bilbao Crystallographic Server [31]. The mechanical representations are:

$$\Gamma_{22} = 2A_{1g} + 2A_{2g} + 2B_{1g} + 2B_{2g} + 2E_g + 2A_{2u} + 2B_{2u} + 4E_u \quad (1)$$

Table 1: Optimized structure parameters of Sn_4Se_4 and Sn_6Se_6 standalone nanowires calculated with HSE06 hybrid functional. The bond lengths between atoms belonging to the same Sn_2Se_2 (Sn_3Se_3) plane are denoted as "in", and those between atoms from neighboring planes – by "out".

Sn_2Se_2	Distance (Å)
Translation period c	5.708
Sn–Se (in)	2.690
Sn–Sn (in)	3.698
Se–Se (in)	3.909
Sn–Se (out)	2.856

[h]

Sn_6Se_6	Distance (Å)
Translation period c	4.324
Sn–Se (in)	2.647
Sn–Sn (in)	2.698
Se–Se (in)	2.668
Sn–Se (out)	2.664

for the Sn_4Se_4 SnSe nanowire, and

$$\Gamma_{33} = 2A_{1g} + 2A_{2g} + 2B_{2g} + 2E_{1g} + 4E_{2g} + 2A_{2u} + 2B_{1u} + 2B_{2u} + 4E_{1u} + 2E_{2u} \quad (2)$$

for the Sn_6Se_6 hexagonal nanowire. The acoustic modes are $A_{2u} + E_u$ and $A_{2u} + E_{1u}$ for the Sn_4Se_4 and Sn_6Se_6 nanowires, respectively. The near-zero-frequency rigid rotations about c of the Sn_4Se_4 and Sn_6Se_6 wires correspond to modes of A_{2g} symmetry. The other A_{2g} and B_{2u} modes in the Sn_4Se_4 nanowire, as well as the A_{2g}, B_{2g}, B_{1u}, B_{2u}, and E_{2u} modes in the Sn_6Se_6 nanowire are optically silent. The remaining even (g) modes are Raman active:

$$\Gamma_{22\text{Raman}} = 2A_{1g} + 2B_{1g} + 2B_{2g} + 2E_g \quad (3)$$

$$\Gamma_{33\text{Raman}} = 2A_{1g} + 2E_{1g} + 4E_{2g} \quad (4)$$

while the rest of the odd (u) modes possess infrared (IR) activity:

$$\Gamma_{22\mathrm{IR}} = A_{2u} + 3E_u \tag{5}$$

$$\Gamma_{33\mathrm{IR}} = A_{2u} + 3E_{1u} \tag{6}$$

Therefore, accounting for the degeneracy of the representations, eight different frequencies are expected in the Raman spectra of both nanowires. The corresponding number of the infrared active modes is four in the two structures. The calculated frequencies of the Γ-point modes are summarized in Table 2.

In Sn_4Se_4 and Sn_6Se_6 nanowires the A_{1g} and the E_g (E_{1g}) vibrations entail comparable types of atomic displacements. The totally symmetric A_{1g} modes are radial breathing-type modes of the Sn and Se sublattices. The E_g (E_{1g}) modes involve atomic motions along the nanowire axis, and can be defined as shearing deformations of the two atomic sublattices. Table 2 gives the calculated Γ-point vibrational frequencies for the standalone Sn_4Se_4 and Sn_6Se_6 nanowires. The modes of the same symmetry are numbered in an ascending order of their frequencies.

3.1.3 Electronic band structures

Fig. 2 presents the electronic band structures, as well as the full and partial density of states (DOS) calculated with the HSE06 functional for the layered SnSe bulk crystal and the Sn_4Se_4 and Sn_6Se_6-embedded nanowires. Zero energy corresponds to the Fermi energy E_F.

Note that in periodic DFT calculations, the 1D nanowire is placed in the center of a vacuum box of dimensions a, b, c with volume V sufficiently large to neglect inter-wires interactions. In this 3D scheme, the DOS for electrons or phonons of the wire at energy E can be written as:

$$\rho_{3D}(E) = \frac{V}{(2\pi)^3} \int_{-\pi/a}^{\pi/a} \int_{-\pi/b}^{\pi/b} \int_{-\pi/c}^{\pi/c} dk_x dk_y dk_z \delta\left(E - \mathrm{E}(\mathbf{k})\right) \tag{7}$$

Provided that the interaction between periodic replica of the nanowire is negligible, the band energy function E(**k**) is practically dispersionless in the xy-plane, i.e. $E(k) \equiv E(k_z)$, where k_z is the

1D wavevector along the nanowire axis. In this case the equation (7) is transformed into equivalent expression for the 1D density of states of the nanowire:

$$\rho_{1D}(E) = \frac{c}{2\pi} \int_{-\pi/c}^{\pi/c} dk_z \delta\left(E - \mathrm{E}\left(k_z\right)\right) \tag{8}$$

Therefore, the ρ_{1D} values discussed hereafter depend only on translation period c of the wire and are in principle independent of the vacuum box dimension.

[ht]

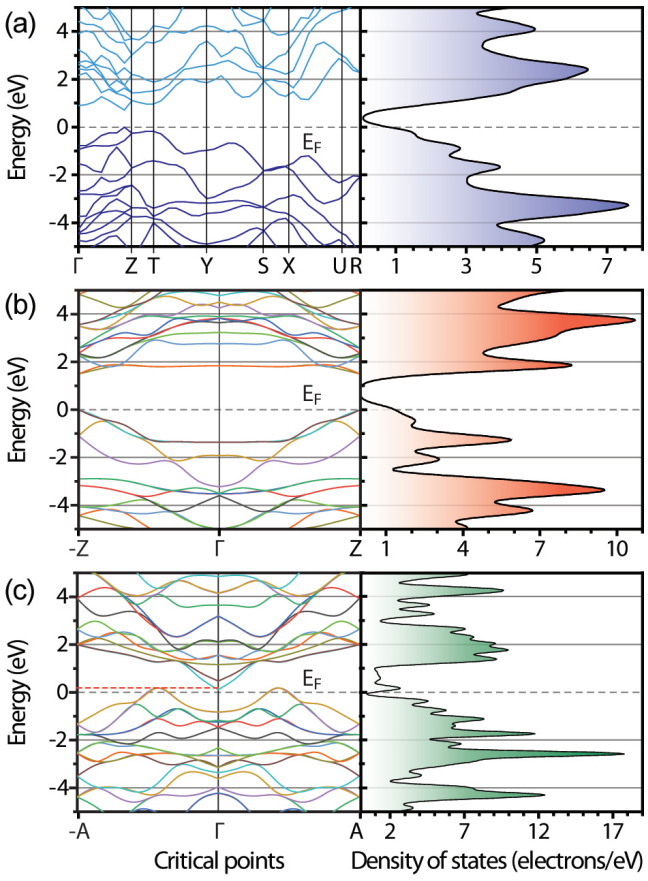

Figure 2: Band structures and density of states of SnSe crystals calculated with DFT at HSE06 level. (a) 3D *Pnma* crystal; (b) 1D square Sn_4Se_4 nanowire along -ZΓZ direction; (c) 1D hexagonal Sn_6Se_6 nanowire along -AΓA directions with spline interpolation. A semimetallic character is revealed above the Fermi level (dotted line). ΓZ and ΓA paths are oriented along the chain direction. The critical points Z and A lie at the edge of the Brillouin zone with coordinate (0,0,1/2). The electronic configuration of Sn atom is $[Kr]5s^24d^{10}5p^2$, s and p orbitals hold valence electrons ($n = 5$).

The band gap in the layered 3D *Pnma* crystal is 0.71 eV, a value relatively close to the experimental

indirect band gap (0.9 eV) and is in the same range as values reported in previous works [32]. The band structure of the Sn_4Se_4 nanowire clearly evidences a direct band gap of 1.49 eV at Z point which should allow optical and resonant transitions in the near IR at about 830 nm. This bandgap energy is higher than those of the *Pnma* crystal (indirect : 0.9 eV, direct : 1.3 eV) and closer to that found by Carter *et al.* [16] for the same infinite rod (1.36 eV) when using the PW91 functional. These two DFT calculations stress that the infinite Sn_4Se_4 nanorod should present a band gap expansion with respect to the bulk layered form.

Here, computations at PBE and HSE levels of theory show that the Sn_6Se_6 nanowire has an almost gapless electronic structure with a small nonzero density of states at the Fermi level. For HSE06 the upper valence branch crosses the Fermi level with a valence band maximum (VBM) at 0.18 eV above E_F while the conduction band minimum (CBM) is only 0.11 eV above E_F at the Γ point (Fig. 2(c)). These VBM and CBM values indicate an energy overlap of about 70 meV suggesting that the Sn_6Se_6 nanowire is a semimetal. To support this prediction, it should be noticed than Yan *et al.* [33] have observed a semiconductor to semimetal transition in powdered SnSe at a pressure of 9 GPa, which has been also verified by their GGA-PBE band structure calculations. The electronic calculations of Yan *et al.* at 9 GPa in the ΓZ direction (Z: (0,0,1/2)) show the same behavior found in the Sn_6Se_6 nanowire: the upper valence band crosses the Fermi level while the lower conduction band goes down to almost zero energy at Γ point.

3.2 Additional Raman bands upon SnSe encapsulation

Fig. 3 presents the unpolarized micro-Raman spectra of a pristine SWCNT sample # 0 and SnSe@SWCNT sample # 1 between 100 and 3000 cm^{-1} obtained at excitation wavelength 785 nm (1.58 eV) for the same power density. In SWCNT spectrum the band of RBM modes is strongly resonant with maximum intensity close to that of the *G* band. The *G* band exhibits an asymmetric shape characteristic of metallic nanotubes contribution and has three components at 1556, 1571, and 1592-1595 cm^{-1} stemming from both metallic (M) and semiconducting (SC) tubes re-

spectively referred to as G^- (LO phonon of M tubes), G^+ (TO phonon of SC tubes), and G^+ (LO phonon of SC tubes) [34,35].

Fig. 4 shows that the RBM frequencies of the pristine nanotubes appear between 150 and 180 cm^{-1} with two resolved peaks at 163 and 173 cm^{-1}. The spectra are normalized to the maximum Raman intensity of low frequency lines for clarity.

Applying the empirical relationship between the RBM frequency in cm^{-1} and tube diameter d [35], $d(nm) = 227/\omega_{\mathrm{RBM}}$, we estimate that these peaks are characteristic for SWCNTs of 1.4 nm and 1.3 nm diameter, respectively. Thus the experimental Raman results confirm that the commercial nanotubes of 1.2-1.7 nm diameter range chosen for the synthesis of our composites are the dominant crystalline structural forms in the samples analyzed here, notwithstanding that other forms may possibly exist but they were not extensively encountered in our study. These diameters can easily accommodate the two types of SnSe 1D nanocrystals discussed in this paper. The estimated diameter of SWCNTs surrounding the SnSe nanowires is:

$$d = d\,(\mathrm{Se\text{-}Se}) + 2\mathrm{r}_{\mathrm{vdW}}\,(\mathrm{Se}) + 2r_{\mathrm{vdW}}\,(\mathrm{C}) \tag{9}$$

where r_{vdW} is the van der Waals radius of the atom and d(Se-Se) is the cross-sectional distance between opposite Se atoms. For optimized geometries of Sn_4Se_4 and Sn_6Se_6 crystals we find d = 1.11 nm and 1.45 nm, respectively. These values correspond well with the diameter estimates from Raman spectra.

Strikingly several novel lines appear at low frequencies in the Raman spectra of SnSe@SWCNT samples # 1, # 2 and # 3 for exciting wavelengths 633 and 785 nm, while the absolute intensity of the RBM and G modes either vanishes or strongly diminishes.

These additional low-frequency bands are located at 108-109, 126-131, 151, 185, 235 cm^{-1} (see Fig. 3 and Fig. 4). All these bands are absent in the pristine nanotubes spectrum (samples # 0). For sample # 1 the signals of nanotube walls are hardly detected in the region between 140 and 180 cm^{-1} and are overlapped by the additional band at 150 cm^{-1}. In sample # 2, the RBM bands are absent.

The supplemental lines appearing for the SnSe@SWCNT samples may result from encapsulation of SnSe in SWCNTs since their relative intensities do not match those of bulk *Pnma* SnSe or $P\bar{3}m1$ $SnSe_2$ crystals at 111 cm^{-1} (E_g) and at 187 cm^{-1} (A_{1g}) as shown in Fig. 4, and therefore do not seem characteristic of remnant tin selenide compounds in between and outside the nanotubes walls [36-41]. It can be inferred that these bands are likely to characterize mainly other phases of tin selenide. This assumption is supported by the changes of the RBM and *G* bands of the SWCNTs in the SnSe@SWCNT nanostructures. The relative intensity of these lines and their moderate HWHM indicate that these crystals are well ordered inside the SWCNT walls. The additional strong bands at 185 and 235 cm^{-1} cannot be ascribed to the SnSe *Pnma* crystal. We found that for 633 nm excitation this compound exhibits Raman bands at 32 (A_g), 55 (B_{1g}), 68 (A_g), 106 (B_{3g}), 129 (A_g), 148 (A_g), and 179 cm^{-1} (very weak) in agreement with previous work [36]. They likely characterize intrinsic features of the nanowires embedded in SWCNT because the occurrence of these bands is predicted in SnSe 1D standalone crystals by the vibrational calculations described hereafter. Our interpretation is also conforted by Raman data of MoTe@SWNT samples acquired by Nagata *et al.* [17]. They found in their samples a Raman line at 255 cm^{-1} that they ascribed to the vibrations of the embedded MoTe nanowires. Similarly to our experiments, their observation was carried out at a laser power of 347 μW using the same equipment and the He-Ne 633 nm laser line. Since Sn_6Se_6 and MoTe nanowires have close structures, their Raman experiment suggests that the SnSe nanowires vibrational Raman lines should lie in the same range of frequencies.

3.3 Analysis of *G* bands

At higher frequencies the G^-, G^+ modes of the SnSe@SWCNT samples are still visible but are considerably reduced in intensity (Fig. 3). The profile of the *G* band remains strongly asymmetric with a shift of the two G^+ components towards higher energies by about 4 cm^{-1} at 1578, and 1596 cm^{-1}, respectively (blueshift). There is an overall diminution of the spectral signal-to-noise ratio in samples # 1 and # 2 and the relative intensity of the G^+ TO line located at 1578 cm^{-1} is weaker. The relative intensity of the *D* band is enhanced with respect to that of *G* band indicating that more

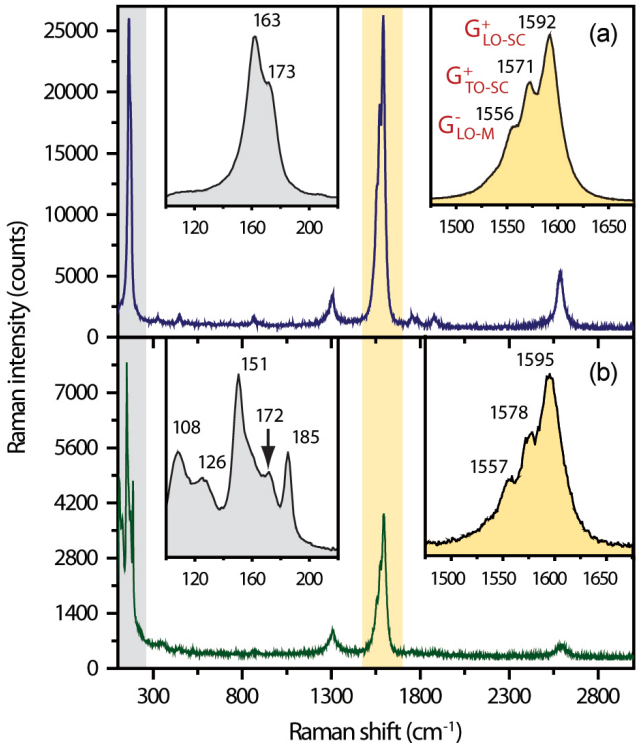

[ht]

Figure 3: Experimental Raman spectra of pristine SWCNT (NanoIntegris 99% pure sample # 0), a), and SnSe@SWCNT sample # 1, b) recorded between 100 and 3000 cm^{-1} at excitation 1.58 eV (785 nm) and for the same laser power. The insets show sub-band features in the *G* band for pristine sample and RBM frequency region for the composite.

defects are present in the encapsulating nanotube walls. Finally, the second order G' ($2D$) band located at 2586 cm^{-1} in pristine SWCNTs shifts towards 2600 cm^{-1} and weakens in relative intensity in the SnSe@SWCNT samples. The blueshift of the G and G' Raman bands upon encapsulation of SnSe and the overall intensity damping of the spectrum indicates a p-type doping of the SWCNT template [42,43].

This experimental result is in line with DFT calculations of work functions (WF) carried out on the SnSe standalone nanowires and presented in the Supporting Information. For Sn_4Se_4, the bonding energies of HOMO (4.574 eV) and LUMO (3.385 eV) are lower than the known WF of SWCNT (~4.8 eV) and near the WF of graphene (4.6 eV). The calculated WF of Sn_4Se_4, which refers to the Fermi level situated in the middle between HOMO and LUMO, is 3.98 eV. Thus, if there is a charge transfer between the Sn_4Se_4 and the SWCNT, the CNT should accept electrons, i.e. become n-doped. However, the calculated WF of Sn_6Se_6 is 5.412 eV, significantly larger than that of

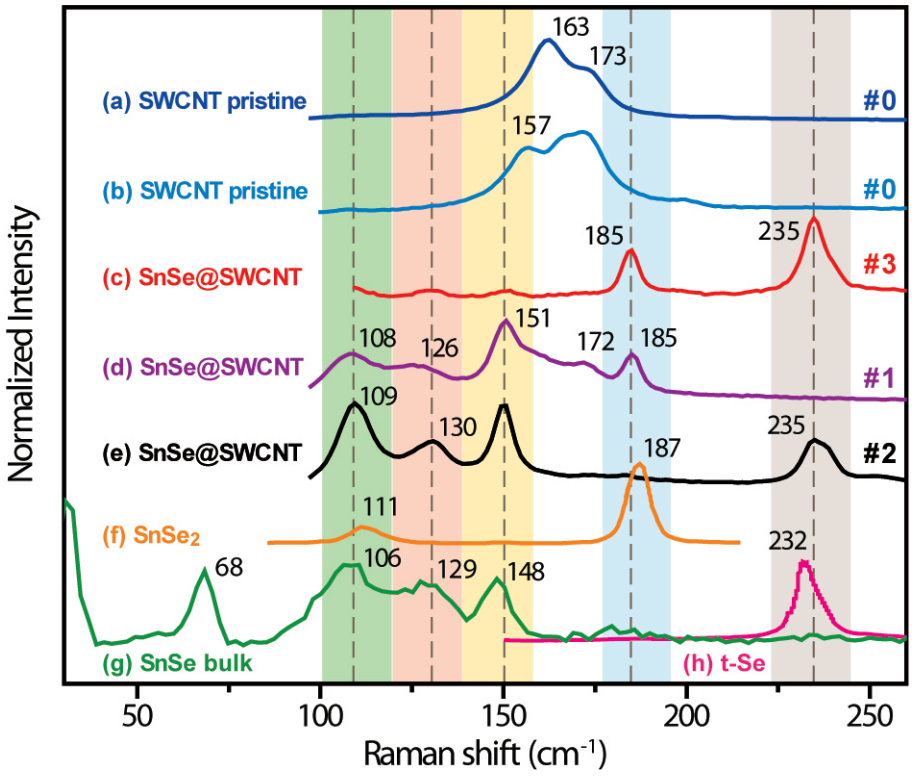

[ht]

Figure 4: Low frequency Raman spectra of pristine SWCNT, SnSe filled SWCNT, and tin selenide compounds. Pristine SWCNT sample # 0 (NanoIntegris 99% pure) at λ_{exc} = 785 nm (1.58 eV) (a) and λ_{exc} = 633 nm (1.96 eV) (b); (c) SnSe@SWCNT (sample # 3) λ_{exc} = 633 nm ; (d,e) SnSe@SWCNT (samples # 1 # 2), λ_{exc} = 785 nm ; (f) $SnSe_2$ $P\bar{3}m1$ crystal, λ_{exc} = 785 nm; (g) SnSe *Pnma* crystal λ_{exc} = 633 nm; (h) for information: trigonal Se $P3_121$ crystal, λ_{exc} = 633 nm. Spectra (f,h) are taken from literature.

SWCNT. Therefore, in this case we can rationalize that the CNT should oppositely give electrons to the Sn_6Se_6 nanowire, i.e. be *p*-doped. Thus the spectral signatures of a *p*-doping (or hole doping) of SWCNTs could be fingerprints for presence of Sn_6Se_6 nanowires encapsulated in the nanotubes. One can anticipate that the experimental shape of the *G* band can be fitted by adding together two Lorentzian functions for G^+ LO and G^+ TO lines and a Breit-Wigner-Fano (BWF) line shape for the G^- LO sub-band [44]. This choice is supported by the fact that the G^- LO sub-band is supposed to stem from the tangential vibrational modes of metallic SWCNTs [45] and therefore may acquire a BWF profile. By theoretical predictions Gayen *et al.* [46] also anticipated that a BWF lineshape might be observed on the *G* band when semiconducting SWNTs are filled with donor

atoms. The BWF lineshape writes as:

$$I(\omega) = \frac{I_0 \left[1 + (\omega - \omega_{\mathrm{BWF}})/q\Gamma\right]^2}{1 + \left[(\omega - \omega_{\mathrm{BWF}})/\Gamma\right]^2} \tag{10}$$

where I_0 is the maximum intensity of the line, ω_{BWF} the resonance frequency, Γ the spectral width, and $1/q$ the asymmetry parameter.

Fig. 5 shows the experimental Raman spectra fitted with a Breit-Wigner-Fano and two Lorentzians functions obtained for pristine SWCNT (sample # 0), and the two SnSe@SWCNT samples (# 1 and # 2) presented above. Several modifications of the Raman spectra occur upon encapsulation (see Fig. 5):

(i) The three components of the tangential G band features undergo both shape and energy changes. The BWF component corresponding to the G^- LO mode of metallic tubes is more asymmetric with an upshift of about 2 cm^{-1}. The Lorentzian components G^+ TO and G^+ LO of semiconducting tubes are upshifted by 3 to 4 cm^{-1}, and their FWHM increases.

(ii) The integrated intensity ratio of BWF and highest Lorentzian components ($I_{\mathrm{BWF}}/I_{G^+LO}$) diminishes after encapsulation due to the broadening of the G^+ LO feature.

(iii) The asymmetry parameter $|1/q|$ is much higher for encapsulating samples than for the pristine sample indicating that metallicity of tubes is increased in these nanomaterials as expected from the calculated band structures. The value found after fitting for pristine SWCNT is 0.196, close to that of Ref. [44] (0.23) while for samples # 1 and # 2, it increases to 0.380, and 0.306, respectively.

The interference part of the BWF profile in eq. 11, i.e. the BWF interference function [47], is expressed as

$$I'(\omega) = \frac{2\left(\omega - \omega_{\mathrm{BWF}}\right)/q\Gamma}{1 + \left[\left(\omega - \omega_{\mathrm{BWF}}\right)/\Gamma\right]^2} \tag{11}$$

It characterizes the interaction between the vibrational mode and a constant continuum of electronic excitations. A plot of this function shows that the electron-phonon interaction between G^-

LO and G^+ TO Raman contributions in the encapsulating samples is stronger, showing that metallicity of these samples is higher than in the pristine carbon nanotubes.

In addition, the difference of interference functions between SnSe@ SWCNT and pristine SWCNT samples indicates that a stronger BWF interaction occurs in the former as exemplified by Fig. 5(b) (red contour) whose signal is positive in the range 1540-1565 cm^{-1} and whose maximum is located near the frequency of the BWF component in SWCNT (1555 cm^{-1}) and SnSe@SWCNT samples. As a consequence, the BWF interference does not affect the G^+ LO mode in SnSe@SWCNT but may have a small influence on the frequency of the G^+ TO mode. Overall, the frequency hardening of the G^- band between pristine and encapsulating nanotubes is mainly due to the encapsulated crystals modifying the mechanical properties of the nanotubes walls.

In a previous work, CNTs have been decorated by SnSe crystals for applications in Li-battery electrodes [48]. In this case there no encapsulation of the chalcogenide. Raman spectra recorded on these hybrids exhibit *D* and *G* band profiles different than those we have observed in this work. Aside our HRTEM investigation, this is a hint that the CNTs in our samples are not covered by the chalcogenide.

3.4 Phonons of the encapsulated nanowires

The phonon dispersions and DOS have been calculated at HSE level of theory for the two SnSe standalone nanowires and for the *Pnma* SnSe crystal for comparison (Fig. 6). Additionally, the partial phonon DOS unveils the individual contribution of Sn and Se atoms to the vibrational spectrum.

The partial phonon DOS of the SnSe *Pnma* crystal shows that the main Sn vibrations occurring between 60-72 cm^{-1}, accompanied by additional modes at 176 and 194 cm^{-1}, with small densities at 109 and 210 cm^{-1}. The Se vibrations are mainly centered at 180 and 194 cm^{-1} with smaller densities at 59, 70, 108 and 209 cm^{-1}.

The partial DOS of the Sn_4Se_4 nanowire reveal strong differences with the 3D bulk crystal. The DOS exhibit more featured spectra with large contributions at 30, 54, 72, 96, 113, 149, 192 cm^{-1}

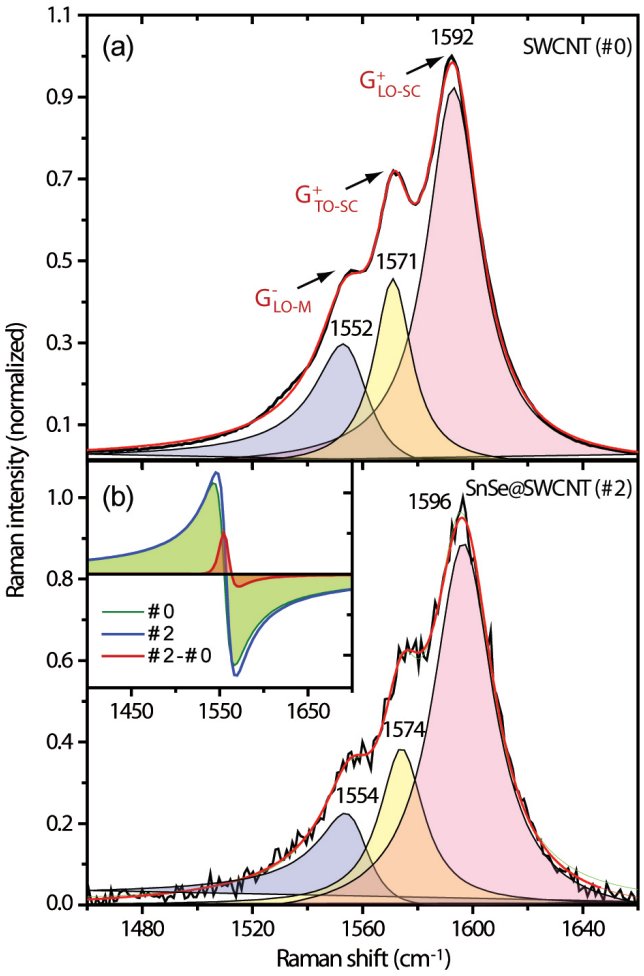

[ht]

Figure 5: Normalized experimental Raman spectra of pristine and SnSe filled SWCNT fitted with a BWF function (G^- band) and two Lorentzian functions (G^+ TO and G^+ LO bands). (a): pristine SWCNT (NanoIntegris 99% pure, sample # 0). (b): SnSe@SWCNT (sample # 2). In inset: BWF interference functions for SWCNT (green contour), sample # 2 (solid blue line), and differences of BWF interference functions between sample # 2 and SWCNT (red contour).

for the Sn atom, and at 31, 54, 72, 124, 150, 174, 192 cm^{-1} for the Se atom. Therefore, one can conclude that the phonon DOS of the standalone Sn_4Se_4 nanowire distinguishes from the bulk crystal with several specific vibrational signatures appearing around 30, 54 and 150 cm^{-1} and possibly recognizable in the experiment.

On the other hand, the vibrational frequencies at Γ point for the Sn_4Se_4 and Sn_6Se_6 1D nanowires are compiled in Table 2 for the HSE functional. In the case of the Sn_4Se_4 wire, the calculated frequencies are within 7 - 12 cm^{-1} (i.e. either downshifted or upshifted) with respect to the observed ones in the spectra of the two SnSe@SWCNT samples. The modes computed at 181 and 194 cm^{-1}

are pure radial SnSe breathing vibrations related to an experimental line appearing between 185 and 187 cm^{-1} with relatively strong intensity in the Raman spectrum of filled samples.

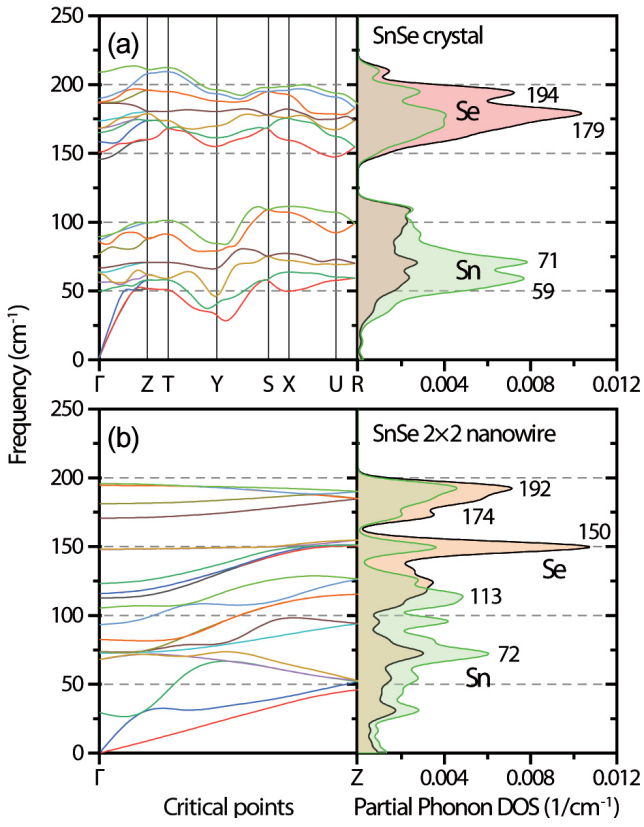

[ht]

Figure 6: Calculated phonon dispersions and density of states of SnSe crystals: (a) 3D *Pnma* crystal; (b) 1D $p4_2/mmc$ Sn_4Se_4 crystal with dominating flat bands.

The computed phonon DOS ρ_{1D} for the Sn_4Se_4 wire shows several features at 117, 150, 174, and 192 cm^{-1}which are near the additional Raman lines found in experimental spectra (Fig. 6(b)). The phonon DOS shows that the heavier Sn atoms and the lighter Se atoms contribute mainly to the acoustic and optical modes, respectively. In particular, the maximum DOS at 150 and 192 cm^{-1} corresponds to unique flat bands of the phonon dispersion dominated by Se atoms which may lead to low lattice thermal conductivity in the Sn_4Se_4 nanowire due to the anharmonic scattering of phonons. Meanwhile the group velocity along $\Gamma-Z$ direction seems lower in the Sn_4Se_4 nanowire than in the bulk, consistent with flattening of the phonon dispersion curves in this nanowire. In the case of the Sn_6Se_6 wire, there is also a very good match between calculated and experimental Raman frequencies at the zone center (Table 2).

Table 2: Calculated Γ-point frequencies (cm^{-1}) for Sn_4Se_4 and Sn_6Se_6 nanowires.

Sn_4Se_4 (2×2)								
A_{1g}	A_{2g}	B_{1g}	B_{2g}	E_g	A_{2u}	B_{1u}	B_{2u}	E_u
	29	73	83	68			93	74
					105			
113				116			123	
	148		148					
								171
181		194						196
Sn_6Se_6								
A_{1g}	A_{2g}	B_{2g}	E_{1g}	E_{2g}	A_{2u}	B_{1u}+B_{2u}	E_{1u}	E_{2u}
	22							
	83		83					90
		121		108		112	110	
				135	135		132	
163		186	172	150		162		181
						230		222
246				254				

The highest calculated Raman frequencies at the HSE level occur at 194 (B_{1g}) and 254 cm^{-1} (B_{2g}) for the Sn_4Se_4 and Sn_6Se_6 wires, respectively, while the highest experimental Raman frequency not assignable to SWCNTs is found at 235 cm^{-1} in the Raman spectrum of one of the SnSe@SWCNT composites. Regarding this band, we note also that phonon calculation of a trigonal-Se crystal with fixed cell parameters using PBE and HSE06 functionals gives a Raman active mode at 227 cm^{-1}, and 236 cm^{-1}, respectively, close to the experimental value at 235 cm^{-1} (A_1 mode) [49,50]. Despite that this Raman band observed at 235 cm^{-1} might be the signature of t-Se presence in the samples [51,52], there is no other analytical evidence of this material in the composite or of its formation above the melting point of SnSe during the synthesis process. Therefore, we ascribe the 235 cm^{-1} line to Sn_6Se_6 embedded nanowires.

Finally, the phonon dispersion in the 3D SnSe crystal shows a phonon gap of about 50 cm^{-1} in all directions of the BZ with phonon branches clearly segregated into two groups of frequencies centered at 70 and 180 cm^{-1} (Fig. 6(a)). By comparison, the phonon branches of the 1D Sn_4Se_4 nanowire do not extend beyond 200 cm^{-1} with a phonon gap of about 20 cm^{-1} along Γ-Z between 150 and 175 cm^{-1} (Fig. 6(b)). While the phonons energies at $q > 0$ in the Sn_6Se_6 nanowire could

not be calculated at HSE level with FD method due to limitations stemming from the large size of the supercell, the $q = 0$ phonons frequencies have been determined and are reported in Table 2. The absence of negative frequencies in the vibrational calculations and phonon dispersion relations shows that the standalone 1D nanowires Sn_4Se_4 and Sn_6Se_6 are structurally stable.

3.5 Nanotube-nanowire interaction

To estimate the nanotube interaction with the encapsulated SnSe crystals we considered the case of the embedded Sn_6Se_6 nanowire. The cross section of the DFT optimized standalone Sn_6Se_6 crystal is systematically expanded compared to the crystal diameter of ~6.2 Å revealed by HRTEM. In fact, the Sn_6Se_6 crystals can fit into (9,9) tubes of 1.22 nm diameter, which infers for a substantial compressive stress on the Sn_6Se_6 crystal as the Se distance to the SWCNT wall is ~3.0 Å, i.e. smaller than the sum of Sn and C van der Waals radii ~3.5 Å.

Table 3: Lennard-Jones parameters of Se$\cdots$C interaction. Forces on the Se atom in the composite SnSe@SWCNT(9,9) and on the Sn_6Se_6 standalone nanowire after optimization (in eV/Å).

[ht]

	Cartesian coordinates of forces			Cross-section
	x	y	z	σ (Å)
Sn_6Se_6	-0.00044	0	0	7.302
Se in (9,9) tube	0.48822	0.02555	-0.00259	
	Lennard-Jones parameters			Distance
	E (eV)	r_0 (Å)	$R_{\min}$–$R_{\max}$ (Å)	d (Å)
Se$\cdots$C	0.020	3.52	0.5 – 10	2.98

To estimate the nanotube interaction with the encapsulated Sn_6Se_6 crystal, we derived a simple model involving a Lennard-Jones (LJ) potential for a pair of non-bonded Se and C atoms:

$$V(r) = -\epsilon \left[(r_0/r)^{12} - 2(r_0/r)^6 \right] \tag{12}$$

where ϵ corresponds to the cohesion energy, and r_0 - to the equilibrium distance between the atoms, which is usually taken as a sum of their van der Waals radii. Due to the two-body and short-range nature of LJ interaction, it is sufficient to calculate on a single protruding Se atom the resul-

tant force applied by a finite segment of a (9,9) SWCNT (5 unit cells in our case). The as calculated force on Se atoms was compared to that exerted on the Se atom in a Sn_6Se_6 crystal during optimization *in vacuo*. We established that for realistic Se$\cdots$C interaction parameters (Table 3) the intra-nanowire expansion force obtained from the DFT calculations for the standalone Sn_6Se_6 1D crystal is compensated by a repulsive LJ force of 0.488 eV/Å at a distance of ~2.98 Å between the Se atoms and the SWCNT wall. This fact evidences that although Sn_6Se_6 is stable in vacuo, its geometry in encapsulated form is influenced by the pressure exerted from the surrounding SWCNT. On the other hand, the force constant corresponding to the LJ interaction, being of order of $72\epsilon/r_0^2 \approx 0.116$ eV/Å^2, is too small to affect significantly the vibrational frequencies of the Sn_6Se_6 crystal, where typical Sn-Se force constants are more than an order of magnitude larger. Therefore, the normal mode analysis based on DFT calculations for the standalone crystal is representative for the encapsulated crystal, as well.

4 Conclusion

We have performed a combined experimental and theoretical study of SnSe@SWCNT composites where periodic DFT calculations support the Raman spectra recorded on several samples. At the HSE level of theory, the Sn_4Se_4 1D crystal exhibits a direct gap larger than that of the 3D crystal allowing direct optical excitations in the near infrared. In contrast, the band structure of the 1D hexagonal crystal is typical to that of a semimetal due to the overlap at the Fermi level of the upper valence band and the lower conduction band with small density of states at the Fermi energy. The calculated vibrational frequencies of the two standalone 1D SnSe nanowires are consistent with supplemental Raman lines observed in the Raman spectra of SnSe@SWCNT composites. Additionally, Raman experiments show that the encapsulated SnSe nanowires modify the electronic and vibrational properties of the surrounding SWCNT walls.

Supporting Information

Supporting Information File 1:

File Name: snse-nano_SI.pdf

File Format: PDF

Title: Workfunction and projected electronic density of states of the stand-alone tin selenide nanowires.

Acknowledgements

We acknowledge Dr. C. Ewels for helpful discussions. This work was supported by the French-Bulgarian bilateral exchange program through Campus France PHC RILA Grants No. 38661ZF and No. DHTC France 01/10/09.05.2017 and by Contract No. KP-06-N38/10/6.12.2019 of the Bulgarian National Science Fund; and by the NATO SPS MYP program N° 985481 "Quantum sensor". JS is indebted to the EPSRC for additional support from EPSRC Grants EP/I033394/1 and EP/R019428/1. This research used resources of Centre de Calcul Intensif des Pays de la Loire (CCIPL), Nantes, France.

ORCID iDs

N Kalashnyk https://orcid.org/0000-0003-0314-6091

E Faulques https://orcid.org/0000-0002-7761-8509

J. Sloan https://orcid.org/0000-0001-8612-7456

V G Ivanov https://orcid.org/0000-0001-5405-8847

References

1. Zhang, C.; Yan, Y.; Sheng Zhao, Y.; Yao, J. *Annu. Rep. Prog. Chem., Sect. C: Phys. Chem.* **2013**, *109*, 211. doi:10.1039/c3pc90002a.

2. Dasgupta, N. P.; Sun, J.; Liu, C.; Brittman, S.; Andrews, S. C.; Lim, J.; Gao, H.; Yan, R.; Yang, P. *Adv. Mater.* **2014**, *26* (14), 2137–2184. doi:10.1002/adma.201305929.

3. Velea, A.; Opsomer, K.; Devulder, W.; Dumortier, J.; Fan, J.; Detavernier, C.; Jurczak, M.; Govoreanu, B. *Sci Rep* **2017**, *7* (1), 8103. doi:10.1038/s41598-017-08251-z.

4. Matthews, P. D.; McNaughter, P. D.; Lewis, D. J.; O'Brien, P. *Chem. Sci.* **2017**, *8* (6), 4177–4187. doi:10.1039/C7SC00642J.

5. Jing, Y.; Liu, B.; Zhu, X.; Ouyang, F.; Sun, J.; Zhou, Y. *Nanophotonics* **2020**, *9* (7), 1675–1694. doi:doi:10.1515/nanoph-2019-0574.

6. Jia, T.; Feng, Z.; Guo, S.; Zhang, X.; Zhang, Y. *ACS Appl. Mater. Interfaces* **2020**, *12* (10), 11852–11864. doi:10.1021/acsami.9b23297.

7. Gao, M.-R.; Xu, Y.-F.; Jiang, J.; Yu, S.-H. *Chem. Soc. Rev.* **2013**, *42* (7), 2986. doi:10.1039/c2cs35310e.

8. Shi, W.; Gao, M.; Wei, J.; Gao, J.; Fan, C.; Ashalley, E.; Li, H.; Wang, Z. *Adv. Sci.* **2018**, *5* (4), 1700602. doi:10.1002/advs.201700602.

9. Zhao, L.-D.; Lo, S.-H.; Zhang, Y.; Sun, H.; Tan, G.; Uher, C.; Wolverton, C.; Dravid, V. P.; Kanatzidis, M. G. *Nature* **2014**, *508* (7496), 373–377. doi:10.1038/nature13184.

10. Kumar, M.; Rani, S.; Singh, Y.; Gour, K. S.; Singh, V. N. *RSC Adv.* **2021**, *11*, 6477–6503. doi:10.1039/D0RA09807H.

11. Saito, R.; Dresselhaus, G.; Dresselhaus, M. S. *Physical Properties of Carbon Nanotubes*; Published by Imperial College and distributed by World Scientific Publishing Co., 1998; doi:10.1142/p080.

12. Ajayan, P. M.; Zhou, O. Z. *Applications of Carbon Nanotubes In: Dresselhaus M.S., Dresselhaus G., Avouris P. (eds) Carbon Nanotubes. Topics in Applied Physics, vol 80*; Springer, Berlin, Heidelberg, 2001; doi:10.1007/3-540-39947-X_14.

13. Schnorr, J. M.; Swager, T. M. *Chemistry of Materials* **2011**, *23* (3), 646–657. doi:10.1021/cm102406h.

14. Carter, R.; Sloan, J.; Kirkland, A. I.; Meyer, R. R.; Lindan, P. J. D.; Lin, G.; Green, M. L. H.; Vlandas, A.; Hutchison, J. L.; Harding, J. *Phys. Rev. Lett.* **2006**, *96*, 215501. doi:10.1103/PhysRevLett.96.215501.

15. Giusca, C. E.; Stolojan, V.; Sloan, J.; Börrnert, F.; Shiozawa, H.; Sader, K.; Rümmeli, M. H.; Büchner, B.; Silva, S. R. P. *Nano Lett.* **2013**, *13* (9), 4020–4027. doi:10.1021/nl4010354. PMID: 23984706

16. Carter, R.; Suyetin, M.; Lister, S.; Dyson, M. A.; Trewhitt, H.; Goel, S.; Liu, Z.; Suenaga, K.; Giusca, C.; Kashtiban, R. J.; Hutchison, J. L.; Dore, J. C.; Bell, G. R.; Bichoutskaia, E.; Sloan, J. *Dalton Trans.* **2014**, *43* (20), 7391–7399. doi:10.1039/C4DT00185K.

17. Nagata, M.; Shukla, S.; Nakanishi, Y.; Liu, Z.; Lin, Y.-C.; Shiga, T.; Nakamura, Y.; Koyama, T.; Kishida, H.; Inoue, T.; Kanda, N.; Ohno, S.; Sakagawa, Y.; Suenaga, K.; Shinohara, H. *Nano letters* **2019**, *19* (8), 4845—4851. doi:10.1021/acs.nanolett.8b05074.

18. Slade, C. A.; Sanchez, A. M.; Sloan, J. *Nano Lett.* **2019**, *19* (5), 2979–2984. doi:10.1021/acs.nanolett.9b00133.

19. Lin, J.; Cretu, O.; Zhou, W.; Suenaga, K.; Prasai, D.; Bolotin, K. I.; Cuong, N. T.; Otani, M.; Okada, S.; Lupini, A. R.; Idrobo, J.-C.; Caudel, D.; Burger, A.; Ghimire, N. J.; Yan, J.; Mandrus, D. G.; Pennycook, S. J.; Pantelides, S. T. *Nature Nanotechnology* **2014**, *9* (6), 436–442. doi:10.1038/nnano.2014.81.

20. Koh, A. L.; Wang, S.; Ataca, C.; Grossman, J. C.; Sinclair, R.; Warner, J. H. *Nano Letters* **2016**, *16* (2), 1210–1217. doi:10.1021/acs.nanolett.5b04507. PMID: 26785319

21. Çak ır, D.; Durgun, E.; Gülseren, O.; Ciraci, S. *Phys. Rev. B* **2006**, *74*, 235433. doi:10.1103/PhysRevB.74.235433.

22. Murugan, P.; Kumar, V.; Kawazoe, Y.; Ota, N. *Nano Letters* **2007**, *7* (8), 2214 2219. doi:10.1021/nl0706547. PMID: 17625902

523 23. Spencer, J. H.; Nesbitt, J. M.; Trewhitt, H.; Kashtiban, R. J.; Bell, G.; Ivanov, V. G.;
524 Faulques, E.; Sloan, J.; Smith, D. C. *ACS Nano* **2014**, *8* (9), 9044–9052. doi:10.1021/
525 nn5023632.

526 24. Ivanov, V. G.; Kalashnyk, N.; Sloan, J.; Faulques, E. *Phys. Rev. B* **2018**, *98* (12), 125429. doi:
527 10.1103/PhysRevB.98.125429.

528 25. Clark, S. J.; Segall, M. D.; Pickard, C. J.; Hasnip, P. J.; Probert, M. I. J.; Refson, K.;
529 Payne, M. C. *Zeitschrift für Kristallographie - Crystalline Materials* **2005**, *220* (5/6), year.
530 doi:10.1524/zkri.220.5.567.65075.

531 26. Hummer, K.; Harl, J.; Kresse, G. *Phys. Rev. B* **2009**, *80* (11), 115205. doi:10.1103/PhysRevB.
532 80.115205.

533 27. Clark, S. J.; Robertson, J. *Phys. Rev. B* **2010**, *82* (8), 085208. doi:10.1103/PhysRevB.82.
534 085208.

535 28. Kim, B. G.; Jo, J.; Cheong, S. *Journal of Solid State Chemistry* **2013**, *197*, 134–138. doi:https:
536 //doi.org/10.1016/j.jssc.2012.08.047.

537 29. Andriotis, A. N.; Richter, E.; Menon, M. *Phys. Rev. B* **2016**, *93*, 081413. doi:10.1103/
538 PhysRevB.93.081413.

539 30. Okazaki, A.; Ueda, I. *Journal of the Physical Society of Japan* **1956**, *11* (4), 470–470. doi:10.
540 1143/JPSJ.11.470.

541 31. Kroumova, E.; Aroyo, M. I.; Perez-Mato, J. M.; Kirov, A.; Capillas, C.; Ivantchev, S.;
542 Wondratschek, H. *Phase Transitions* **2003**, *76* (1-2), 155–170. doi:10.1080/
543 0141159031000076110.

544 32. Das, A.; Kumar, A.; Banerji, P. *Journal of Physics: Condensed Matter* **2020**, *32* (26), 265501.
545 doi:10.1088/1361-648x/ab7ad8.

546 33. Yan, J.; Ke, F.; Liu, C.; Wang, L.; Wang, Q.; Zhang, J.; Li, G.; Han, Y.; Ma, Y.; Gao, C. *Phys.*
547 *Chem. Chem. Phys.* **2016**, *18* (6), 5012–5018. doi:10.1039/C5CP07377D.

548 34. Kharlamova, M. V. *Journal of Spectroscopy* **2015**, *2015*, 1–8. doi:10.1155/2015/653848.

549 35. Araujo, P. T.; Maciel, I. O.; Pesce, P. B. C.; Pimenta, M. A.; Doorn, S. K.; Qian, H.;
550 Hartschuh, A.; Steiner, M.; Grigorian, L.; Hata, K.; Jorio, A. *Phys. Rev. B* **2008**, *77* (24),
551 241403. doi:10.1103/PhysRevB.77.241403.

552 36. Chandrasekhar, H. R.; Humphreys, R. G.; Zwick, U.; Cardona, M. *Phys. Rev. B* **1977**, *15* (4),
553 2177–2183. doi:10.1103/PhysRevB.15.2177.

554 37. Li, X.-Z.; Xia, J.; Wang, L.; Gu, Y.-Y.; Cheng, H.-Q.; Meng, X.-M. *Nanoscale* **2017**, *9* (38),
555 14558–14564. doi:10.1039/C7NR05047J.

556 38. Xu, X.; Song, Q.; Wang, H.; Li, P.; Zhang, K.; Wang, Y.; Yuan, K.; Yang, Z.; Ye, Y.; Dai, L.
557 *ACS Appl. Mater. Interfaces* **2017**, *9* (14), 12601–12607. doi:10.1021/acsami.7b00782.

558 39. Liu, F.; Parajuli, P.; Rao, R.; Wei, P. C.; Karunarathne, A.; Bhattacharya, S.; Podila, R.; He, J.;
559 Maruyama, B.; Priyadarshan, G.; Gladden, J. R.; Chen, Y. Y.; Rao, A. M. *Phys. Rev. B* **2018**,
560 *98* (22), 224309. doi:10.1103/PhysRevB.98.224309.

561 40. Xu, H.; Xing, J.; Huang, Y.; Ge, C.; Lu, J.; Han, X.; Du, J.; Hao, H.; Dong, J.; Liu, H.
562 *Nanoscale Research Letters* **2019**, *14* (1), 17. doi:10.1186/s11671-019-2850-0.

563 41. Kang, M.; Rathi, S.; Lee, I.; Li, L.; Khan, M. A.; Lim, D.; Lee, Y.; Park, J.; Pham, A. T.;
564 Duong, A. T.; Cho, S.; Yun, S. J.; Kim, G.-H. *j nanosci nanotechnol* **2018**, *18* (6), 4243–4247.
565 doi:10.1166/jnn.2018.15189.

566 42. Rao, R.; Pierce, N.; Dasgupta, A. *Applied Physics Letters* **2014**, *105* (7), 073115. doi:10.1063/
567 1.4893698.

568 43. Zafar, Z.; Zafar, A.; Tian, Y.; Cao, Z.; Jin, B.; Shi, Z. *Journal of Raman Spectroscopy* **2017**,
569 *48* (10), 1318–1322. doi:https://doi.org/10.1002/jrs.5239.

570 44. Brown, S. D. M.; Jorio, A.; Corio, P.; Dresselhaus, M. S.; Dresselhaus, G.; Saito, R.;
571 Kneipp, K. *Phys. Rev. B* **2001**, *63* (15), 155414. doi:10.1103/PhysRevB.63.155414.

572 45. Nguyen, K. T.; Gaur, A.; Shim, M. *Phys. Rev. Lett.* **2007**, *98* (14), 145504. doi:10.1103/
573 PhysRevLett.98.145504.

574 46. Gayen, S.; Behera, S. N.; Bose, S. M. *Phys. Rev. B* **2007**, *76*, 165433. doi:10.1103/PhysRevB.
575 76.165433.

576 47. Hasdeo, E. H.; Nugraha, A. R. T.; Dresselhaus, M. S.; Saito, R. *Phys. Rev. B* **2014**, *90* (24),
577 245140. doi:10.1103/PhysRevB.90.245140.

578 48. Luo, X.; Huang, J.; Li, J.; Cao, L.; Cheng, Y.; Guo, L.; Wang, Y.; Qi, H. *Applied Surface Sci-*
579 *ence* **2019**, *491*, 95–104. doi:https://doi.org/10.1016/j.apsusc.2019.06.129.

580 49. Sinha, A. K.; Sasmal, A. K.; Mehetor, S. K.; Pradhan, M.; Pal, T. *Chem. Commun.* **2014**, *50*
581 (99), 15733–15736. doi:10.1039/C4CC08168D.

582 50. Pal, A.; Gohil, S.; Sengupta, S.; Poswal, H. K.; Sharma, S. M.; Ghosh, S.; Ayyub, P. *J. Phys.:*
583 *Condens. Matter* **2015**, *27* (41), 415404. doi:10.1088/0953-8984/27/41/415404.

584 51. Colin, R.; Drowart, J. *Trans. Faraday Soc.* **1964**, *60*, 673–683. doi:10.1039/TF9646000673.

585 52. Vasylenko, A.; Marks, S.; Wynn, J. M.; Medeiros, P. V. C.; Ramasse, Q. M.; Morris, A. J.;
586 Sloan, J.; Quigley, D. *ACS Nano* **2018**, *12* (6), 6023–6031. doi:10.1021/acsnano.8b02261.
587 PMID: 29782147